



**Calhoun: The NPS Institutional Archive**  
**DSpace Repository**

---

NPS Scholarship

Publications

---

1992-04

## Field Feedback Computation of Scattering by 2-D Penetrable Objects

Morgan, Michael A.; Welch, Thaddeus B.

---

IEEE Transactions on Antennas and Propagation, Vol. 40, No. 4, April 1992  
<https://hdl.handle.net/10945/46714>

---

This publication is a work of the U.S. Government as defined in Title 17, United States Code, Section 101. Copyright protection is not available for this work in the United States.

*Downloaded from NPS Archive: Calhoun*



Calhoun is the Naval Postgraduate School's public access digital repository for research materials and institutional publications created by the NPS community. Calhoun is named for Professor of Mathematics Guy K. Calhoun, NPS's first appointed -- and published -- scholarly author.

**Dudley Knox Library / Naval Postgraduate School**  
**411 Dyer Road / 1 University Circle**  
**Monterey, California USA 93943**

<http://www.nps.edu/library>

rotated mesh. In contrast, standard finite differencing uses the unrotated mesh where the spatial differencing is dependent on  $\Delta$ . Thus, even though the number of unknowns is roughly the same in both methods, the resolution and accuracy is lower in the finite element case. As these are second-order methods, the errors differ by a factor of two. This can also be seen by considering the red/black grid decoupling. Since each grid is separate, only half of the total unknowns contribute to each solution, necessarily resulting in lower accuracy.

Grid decoupling also explains the apparent increased stability of these finite element methods when compared with FDTD. The stability limit [2] is larger by a factor of  $\sqrt{2}$  in the finite element case simply because the underlying finite difference mesh is larger by the same amount. Increased stability is obtained at the expense of increased error.

Another consequence of grid decoupling is that care must be used to ensure that both grids are excited equally. As an example, a single  $z$ -directed, magnetic current line source in the  $TE_z$  case will excite only one of the rotated finite difference meshes. The results will be quite perplexing, with every other magnetic field remaining at zero. In less extreme cases, when the current source covers several elements, the two meshes may be excited unequally. This gives rise to a sawtooth pattern when examining the spatial variation of the fields.

The red/black grid decoupling described here only occurs when these finite element methods are applied on a regular mesh. The two grids indeed couple when the mesh is skewed, although the effect of this on overall solution accuracy is unknown. Most practical meshes have large regions which are very nearly orthogonal. From this we infer that there are still two weakly coupled finite difference type meshes underlying the finite element grid which may cause difficulties similar to those described above.

The finite element methods described in [2] and [3] are powerful tools. As illustrated by the results in these papers, these methods can be very effective for a wide range of applications. The grid decoupling problem discussed here though raises serious questions and suggests that other discretizations should be sought which alleviate these difficulties. Two such methods have been developed recently, one using a generalization of the FDTD [4], and the other using a finite volume technique [5], [6]. These methods are not subject to grid decoupling difficulties and are more accurate than the finite element methods developed to date.

#### REFERENCES

- [1] K. S. Yee, "Numerical solution of initial boundary value problems involving Maxwell's equations in isotropic media," *IEEE Trans. Antennas Propagat.*, vol. AP-14, pp. 302-307, May 1966.
- [2] A. C. Cangellaris, C. C. Lin, and K. K. Mei, "Point-matched time domain finite element methods for electromagnetic radiation and scattering," *IEEE Trans. Antennas Propagat.*, vol. AP-35, pp. 1160-1173, Oct. 1987.
- [3] R. L. Lee and N. K. Madsen, "A mixed finite element formulation for Maxwell's equations in the time domain," *J. Comp. Phys.*, vol. 88, pp. 284-304, June 1990.
- [4] R. Holland, "Finite difference solutions of Maxwell's equations in generalized nonorthogonal coordinates," *IEEE Trans. Nucl. Sci.*, vol. NS-30, pp. 4589-4591, Dec. 1983.
- [5] N. K. Madsen and R. W. Ziolkowski, "Numerical solution of Maxwell's equations in the time domain using irregular nonorthogonal grids," *Wave Motion*, vol. 10, pp. 583-596, Dec. 1988.
- [6] N. Madsen and R. W. Ziolkowski, "A three-dimensional modified finite volume technique for Maxwell's equations," *Electromagn.*, vol. 10, pp. 147-161, 1990.

## Field Feedback Computation of Scattering by 2-D Penetrable Objects

Michael A. Morgan and Thaddeus B. Welch

**Abstract**—The field feedback formulation is applied to the solution of time-harmonic plane wave scattering by 2-D penetrable objects of arbitrary shape and composition. A conformal mesh, finite element algorithm is employed in the forward operator construction while a near-field Green's function integration is used in forming the feedback operator. Scattering validations for midresonance sized objects include a circular cylinder, a two-region bisected cylinder, a half-circular cylinder, a semicircular shell and a thin lossy planar strip.

#### INTRODUCTION

Finite element and finite difference methods, to be denoted as *finite methods* [1], produce only local interactions between spatial node fields, which are explicitly related only to their nearest neighbors in space. This local connectivity produces highly sparse matrices in the time-harmonic case, thus allowing the use of numerically efficient algorithms for both memory allocation and linear system inversion.

In contrast, moment method approximated integral equations produce completely filled system matrices which embody interactions between each unknown, on a global basis [2]. Integral equations involving inhomogeneous media require *volume type formulations*, wherein the full matrix generation severely constrains the limits on electrical size. For example, assuming an average node spacing of  $0.1 \lambda$  within the material, the integral equation formulation for scattering by an inhomogeneous dielectric cube having equal side dimensions of  $5 \lambda_0$  and average  $\epsilon_r = 4$  would require filling and solving a  $10^6 \times 10^6$  full matrix system.

Due to the localized interactions and sparse system matrices produced, finite methods have the potential to solve larger, and more complex, electromagnetic problems than can be handled by volume type integral equations. However, finite methods require supplemental conditioning on the outer mesh boundary to ensure correct far-zone behavior of solutions in unbounded regions, whereas integral equation formulations innately control radiation field behavior via the Green's function used. Several approaches to properly terminate the outer mesh boundary in finite methods have been developed over the past three decades. These include the infinite element technique [3], the unimoment method [4], [5], the boundary element method [6], [7], use of radiation boundary condition operators [8]-[10], and the field feedback formulation [11], [12].

#### FIELD FEEDBACK FORMULATION

Time-harmonic ( $e^{j\omega t}$ -suppressed) plane wave scattering by 2-D penetrable objects is being considered, as illustrated in Fig. 1 for the special case of a semicircular shell. Both the structure and the fields are invariant to translations in  $z$ . Two orthogonal, linearly polarized incident plane wave vectors,  $\vec{E}_i^{\text{inc}}$ , are shown. Fields are denoted as transverse magnetic (TM) to  $z$ , and transverse electric (TE) to  $z$ , with respective subscripts  $i = 1$  and 2. Three contours should be noted: the body surface,  $S_B$ , the outer geometrical boundary,  $S_0$ , and a Green's function integration contour,  $S_C$ .

A finite element mesh is used to span  $\Omega$  while conforming to the

Manuscript received February 9, 1990; revised October 17, 1991.  
The authors are with the Electrical and Computer Engineering Department, Naval Postgraduate School, Monterey, CA 93943.  
IEEE Log Number 9107083.

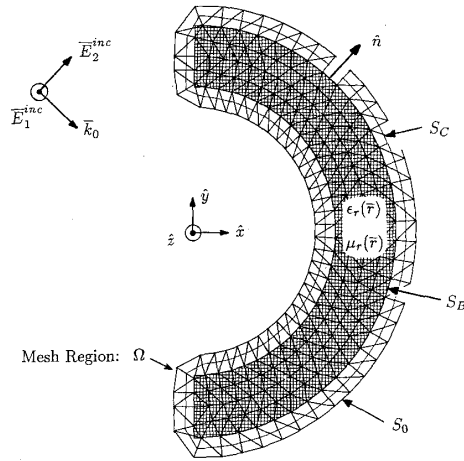


Fig. 1. Scattering problem (semicircular shell) with boundary contours and low density finite element mesh.

body surface, as is depicted in Fig. 1. Complex values for  $\epsilon_r(\vec{r})$  and  $\mu_r(\vec{r})$  may be specified for each triangular element in the mesh to accommodate dissipative loss and spatial inhomogeneity. Nodal field values on  $S_0$  are arranged as an  $M$ -dimensional column array. The finite element solution provides fields at nodes on, and inside of,  $S_B$  produced by specified nodal field values on  $S_0$ .

Three matrix operators are used in the  $F^3$  scattering solution, as illustrated in Fig. 2. The *forward operator*,  $\overline{\mathcal{A}}_i$ , transforms the  $S_0$  boundary node column vector to yield an array of nodal tangential field values, and normal derivative, on the midpoint integration contour,  $S_C$ . This matrix is found by central difference interpolation of the nodal tangential fields on  $S_B$  (due to the finite element solution) and the boundary node tangential fields on  $S_0$ . The *feedback operator*,  $\overline{\mathcal{B}}$ , is formed by numerically evaluating the scattered field at each node on  $S_0$  through an appropriate Green's function integration over  $S_C$  of the tangential field and normal derivative. Scattered fields and radar cross section are found using the  $\overline{\mathcal{C}}$  matrix operator. This matrix is constructed from far-zone Green's function integration of the tangential field and normal derivative on  $S_C$ .

As shown in the  $F^3$  system diagram of Fig. 2, the total field array for nodes on  $S_0$  is  $\vec{F}_0 = \vec{F}_0^{\text{inc}} + \vec{F}_0^{\text{scat}}$ . The forward operator provides the total field array on  $S_C$ , which then produces the scattered field back on  $S_0$ , via the feedback operator. This system has an input-output relationship expressed by the geometric series

$$\begin{aligned} \vec{F}_C &= \overline{\mathcal{A}}_i \cdot [\vec{I} + \overline{\mathcal{Z}}_i + \overline{\mathcal{Z}}_i \cdot \overline{\mathcal{Z}}_i + \overline{\mathcal{Z}}_i \cdot \overline{\mathcal{Z}}_i \cdot \overline{\mathcal{Z}}_i + \cdots] \cdot \vec{F}_0^{\text{inc}} \\ &= \overline{\mathcal{T}}_i \cdot \vec{F}_0^{\text{inc}} \end{aligned} \quad (1)$$

where

$$\overline{\mathcal{Z}}_i = \overline{\mathcal{B}} \cdot \overline{\mathcal{A}}_i \quad (2)$$

is the *closed-loop gain* operator of the  $F^3$  system.

Stability of the feedback system is an important consideration. If the closed-loop gain operator has an array norm  $\|\overline{\mathcal{Z}}_i\| \geq 1$ , then the series in (1) will not converge, indicating an unstable system [13]. For a passive physical scattering system, exhibiting radiation damping and, perhaps, dissipation, it can be argued that  $\|\overline{\mathcal{Z}}_i\| < 1$ . High-Q scattering structures, such as reentrant cavities near resonant frequencies, will store energy via reactive power while rela-

tively little energy loss occurs per oscillation cycle. This resonant behavior will correspond to  $\|\overline{\mathcal{Z}}_i\| \rightarrow 1$ , thus making convergence of (1) slow, if not impractical. Such difficulty in attaining accurate scattering solutions for high-Q structures near resonance is not confined to the  $F^3$  approach, but spans the whole gamut of numerical methods. An advantage of the  $F^3$  is that convergence and accuracy problems for such situations is well defined via closed-loop gain.

Assuming that  $\|\overline{\mathcal{Z}}_i\| < 1$ , the geometric series in (1) can be summed to give the feedback system transfer matrix

$$\overline{\mathcal{T}}_i = \overline{\mathcal{A}}_i \cdot [\vec{I} - \overline{\mathcal{Z}}_i]^{-1} \quad (3)$$

which is the approach employed here. As the system stability is reduced, so is the conditioning of the matrix inversion in (3), as is further discussed in [14].

#### FORWARD OPERATOR

TM and TE vector fields in 2-D can be produced by the scalar Hertz potentials:  $\psi_1(\vec{r}) = E_z(\vec{r})$  and  $\psi_2(\vec{r}) = H_z(\vec{r})$ , [15]. By using wavenumber coordinate normalization,  $x = k_0 x'$  and  $y = k_0 y'$ , Maxwell's curl equations produce vector field generation from

$$\vec{H}(\vec{r}) = \frac{1}{\mu_r} \nabla \psi_1 \times \hat{z} \quad \text{TM case} \quad (4a)$$

$$\vec{E}(\vec{r}) = \frac{1}{\epsilon_r} \nabla \psi_2 \times \hat{z} \quad \text{TE case.} \quad (4b)$$

The Hertz potentials satisfy dual Helmholtz equations in inhomogeneous media,

$$\nabla \cdot [\alpha_i(\vec{r}) \nabla \psi_i(\vec{r})] + \beta_i(\vec{r}) \psi_i(\vec{r}) = 0, \quad \text{for } i = 1, 2 \quad (5)$$

where  $\nabla = \hat{x} \partial / \partial x + \hat{y} \partial / \partial y$ ,  $\alpha_1 = 1/\mu_r(\vec{r})$ ,  $\beta_1 = \epsilon_r(\vec{r})$ , and  $\alpha_2 = 1/\epsilon_r(\vec{r})$ ,  $\beta_2 = \mu_r(\vec{r})$ .

Solution of (5), with specified  $\psi_i$  on  $S_0$ , may be attained using the Euler-Lagrange variational approach, [16]. With specified Dirichlet boundary conditions on  $S_0$ , the  $\psi_i(\vec{r})$  solving (5) also yields the stationary value of the complex functional

$$I_i = \int_{\Omega} \int [\alpha_i(\vec{r}) \nabla \psi_i \cdot \nabla \psi_i - \beta_i(\vec{r}) \psi_i^2] d\Omega. \quad (6)$$

The numerical solution of (6), as used here, employs triangular (simplex) elements for mesh generation inside of  $S_0$ , as shown in Fig. 1. Mesh construction begins by bisecting the object with a segmented curve and then connecting equispaced segments along this bisection to equispaced segments on the body perimeter,  $S_B$ . Outward normal vectors are then generated at each node on  $S_B$  to extend the mesh to the  $S_0$  contour. Finally, triangular elements are inserted between each pair of segments connecting bisection nodes and  $S_0$  nodes. A personal computer graphics CAD program is used to define the body contour,  $S_B$ , and the bisection contour. The mesh is then generated and displayed to the user prior to initiating the finite element solution [12].

Each node of the mesh is assigned an index,  $n$ , and the associated potential at the node is denoted by  $\Psi_i(n)$ . Global node ordering indexes the nonboundary (solution) nodes from 1 to  $N$  and orders the  $M$  boundary nodes on  $S_0$  from  $N+1$  to  $N+M$ . Unit

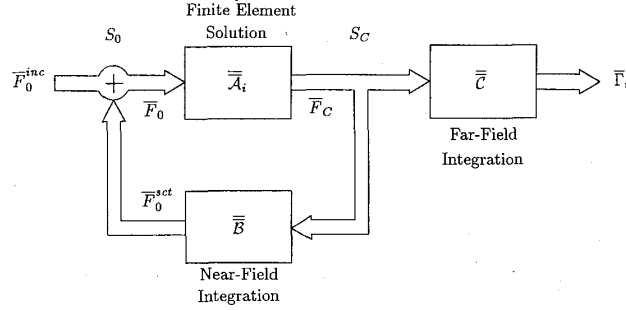


Fig. 2. Field feedback system.

amplitude, piecewise linear basis functions,  $U_n(x, y)$ , are then used to represent the solution within  $S_0$

$$\psi_i(x, y) \doteq \sum_{n=1}^{N+M} \Psi_i(n) U_n(x, y). \quad (7)$$

Substituting (7) into (6) produces the quadratic form,

$$I_i \doteq \sum_{n=1}^{N+M} \sum_{m=1}^{N+M} \Psi_i(n) \Psi_i(m) V(n, m) \quad (8)$$

where the interaction between pairs of nodes is given by

$$V(n, m) = \int_{\Omega} \int [\alpha_i \nabla U_n(x, y) \cdot \nabla U_m(x, y) - \beta_i U_n(x, y) U_m(x, y)] d\Omega. \quad (9)$$

Integration in (9) is straightforward using *area coordinates* [17]. Element integrations are spliced together to form the self ( $m = n$ ) and mutual ( $m \neq n$ ) interaction terms between pairs of nodes.

The stationary value of (8) is found by differentiating with respect to each unknown nodal potential, and nulling the result, to produce a linear equation

$$\sum_{n=1}^N \Psi_i(n) V(n, m) = - \sum_{n=N+1}^{N+M} \Psi_i(n) V(n, m), \quad \text{for } m = 1, \dots, N \quad (10)$$

where known boundary terms appear on the right-hand side. It is important to note that  $V(n, m) = 0$ , unless both the  $n$ th and  $m$ th nodes form vertices of a common triangular element. As a result, the system matrix defined by (10) will be quite sparse. Further, the system matrix can be made to have a triblock structure, thus allowing use of the Ricatti transform algorithm [5].

Recall that the forward matrix operator,  $\mathcal{A}_i$ , transforms the boundary values of  $\psi(s_o)$  to obtain central difference interpolated values for  $\psi_i(s_c)$  and  $\partial\psi_i(s_c)/\partial n$ . Let us denote the column array of  $M$  boundary nodal values on  $S_0$  as

$$\bar{F}_0 = [\Psi(N+1), \Psi(N+2), \dots, \Psi(N+M)]^T \quad (11)$$

where the indexing scheme in (10) is used and the superscript  $T$  indicates transpose. The  $M$  nodal solution values of  $\Psi(n)$  along the  $S_B$  contour are, likewise, reordered to correspond to the nodes on the outer boundary. These are assembled into a column array,  $\bar{F}_B$ . The  $F_C$  column array is composed of  $M$  interpolated values of  $\Psi$ , followed by  $M$  central difference approximated values for the

normal derivative. Denoting the contour separation distance between  $S_B$  and  $S_0$  as  $\Delta R$ , the  $F_C$  array becomes

$$\bar{F}_C = \bar{\mathcal{A}}_i \cdot \bar{F}_0 = \begin{bmatrix} \frac{1}{2} \{\bar{F}_0 + \bar{F}_B\} \\ \frac{1}{\Delta R} \{\bar{F}_0 - \bar{F}_B\} \end{bmatrix}. \quad (12)$$

The finite element method is used to find  $\bar{F}_B$  for any  $\bar{F}_0$  using

$$\bar{F}_B = \bar{\mathcal{Q}}_i \cdot \bar{F}_0 \quad (13)$$

where the  $\bar{\mathcal{Q}}_i$ -matrix is constructed from nodal solution values of  $\psi(s_b)$ , corresponding to individual unit nodal value boundary conditions on  $S_0$ . The forward operator may be found by substituting (13) in (12) and using the  $M \otimes M$  identity matrix,  $\bar{I}$ ,

$$\bar{\mathcal{A}}_i = \begin{bmatrix} \frac{1}{2} \{\bar{I} + \bar{\mathcal{Q}}_i\} \\ \frac{1}{\Delta R} \{\bar{I} - \bar{\mathcal{Q}}_i\} \end{bmatrix}. \quad (14)$$

#### FEEDBACK OPERATOR

The feedback matrix,  $\bar{\mathcal{B}}$ , generates the scattered field portion of  $\bar{F}_0$  from the nodal field terms contained in  $\bar{F}_C$ ,

$$\bar{F}_0^{\text{scat}} = \bar{\mathcal{B}} \cdot \bar{F}_C. \quad (15)$$

Near-field Green's function integrations of the field and its normal derivative over  $S_C$  are required to evaluate the scattered field on  $S_0$ ,

$$\psi_i^{\text{scat}}(s_o) = \int_{S_C} \left[ G(s_o, s_c) \frac{\partial \psi_i(s_c)}{\partial n} - \psi_i(s_c) \frac{\partial G(s_o, s_c)}{\partial n} \right] ds_c \quad (16)$$

where  $\hat{n}$  is the outward unit normal at  $s_c$ , [18]. The 2-D free-space Green's function,

$$G(s_o, s_c) = -\frac{j}{4} H_0^{(2)}(k_0 |\bar{r} - \bar{r}'|) \quad (17)$$

employs the second-kind Hankel function of order zero, where  $R = |\bar{r} - \bar{r}'|$  is the distance between specified  $s_o$  and  $s_c$  contour points.

Numerical integration of (16) uses a subsectional trapezoidal rule. The basis expansion in (7) and its normal derivative, when evaluated on  $S_C$ , are substituted into (16). This provides the scattered field at the  $n$ th nodal point on the  $S_0$  contour,

$$\Psi_i^{\text{scat}}(n) \doteq \sum_{m=1}^M \left[ \frac{\Psi_i^c(m)}{\partial n} \mathcal{B}(n, m+M) - \Psi_i^c(m) \mathcal{B}(n, m) \right]. \quad (18)$$

Feedback matrix elements are given by

$$\mathcal{B}(n, m) = \int_{S_C(m)} \left[ \frac{\partial G(s_o, n, s_c)}{\partial n} u_m(s_c) \right] ds_c \quad (19a)$$

$$\mathcal{B}(n, m + M) = \int_{S_C(m)} [G(s_o, n, s_c) u_m(s_c)] ds_c \quad (19b)$$

where  $u_m(s_c)$  represents  $U_m(x, y)$  on  $S_C$ .

Because of the Green's function singularity, the integrations in (19) require careful consideration for closely spaced points on  $S_o$  and  $S_C$ , (i.e., when  $|n - m|$  is small). An adaptive integration algorithm was developed to maintain uniformly high integration accuracy, independent of source to evaluation point distance. When  $n = m$ , this algorithm typically subdivides the  $S_C(m)$  source region into hundreds of segments. As the distance between points increases, the number of segments is reduced rapidly to a minimum of six. RMS errors of less than 1% were observed for a variety of tests involving circular contour integrations of plane waves and cylindrical harmonics.

#### SCATTERED FIELD GENERATION

The far-zone approximation to the integral in (16) gives the form [18],

$$\psi_i^s(\bar{r}) \doteq \sqrt{\frac{j}{8\pi k_0 r}} e^{-jk_0 r} \gamma_i(\theta) \quad (20)$$

where the pattern function,

$$\gamma_i(\theta) = \int_{S_C} \left[ j \frac{\partial \psi_i(s_c)}{\partial n} + k_0 \hat{n} \cdot \hat{r} \psi_i(s_c) \right] e^{jk_0 \hat{r} \cdot \bar{r}} ds_c \quad (21)$$

depends on direction, as specified by  $\hat{r} = \cos(\theta) \hat{x} + \sin(\theta) \hat{y}$ . The usual far-zone conditions required are: 1)  $k_0 R = k_0 |\bar{r} - \bar{r}'| \gg 1$ ; 2)  $r > D$ , and; 3)  $r > 2D^2/\lambda_0$ , where  $D$  is the maximum 2-D object dimension.

The  $\bar{\mathcal{E}}$ -matrix provides the pattern function in selected directions defined by  $\theta_\alpha$ ,  $\alpha = 1, 2, \dots, K$ ,

$$\bar{\Gamma}_i = [\gamma_i(\theta_1), \gamma_i(\theta_2), \dots, \gamma_i(\theta_K)] = \bar{\mathcal{E}} \cdot \bar{F}_C. \quad (22)$$

Integration in (21) can be approximated by

$$\gamma_i(\theta_\alpha) \doteq \sum_{m=1}^M \left[ \frac{\Psi_i^c(m)}{\partial n} \mathcal{C}(\alpha, m + M) - \Psi_i^c(m) \mathcal{C}(\alpha, m) \right] \quad (23)$$

where the elements of the  $\bar{\mathcal{E}}$ -matrix use far-zone Green's function integrations,

$$\mathcal{C}(\alpha, m) = k_0 \int_{S_C(m)} u_m(s_c) (\hat{n} \cdot \hat{r}_\alpha) e^{jk_0 \hat{r}_\alpha \cdot \bar{r}_\alpha} ds_c \quad (24a)$$

$$\mathcal{C}(\alpha, m + M) = j \int_{S_C(m)} u_m(s_c) e^{jk_0 \hat{r}_\alpha \cdot \bar{r}_\alpha} ds_c. \quad (24b)$$

Bistatic radar cross section per unit length in 2-D, is given by

$$\sigma_i(\theta) = \lim_{r \rightarrow \infty} \frac{2\pi r |\psi_i^s|^2}{|\psi_i^{inc}|^2} = \frac{|\gamma_i(\theta)|^2}{4k_0}. \quad (25)$$

This is easily discretized for directions  $\theta_\alpha$  using the computed  $\bar{\Gamma}_i$  array in (22).

#### VALIDATIONS

Scattering computations made by the  $F^3$  algorithm are compared to alternate numerical solutions for several 2-D penetrable objects.

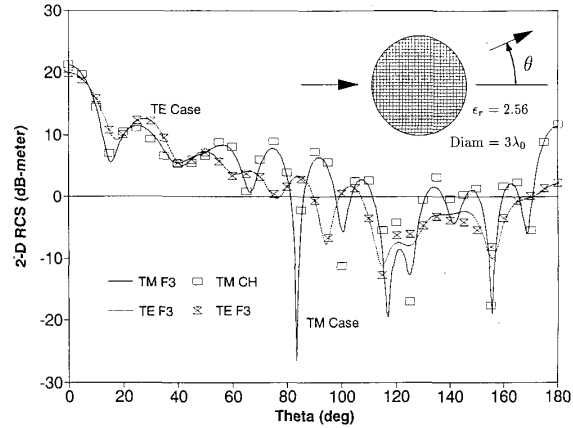


Fig. 3. Comparison of bistatic RCS for a circular dielectric cylinder having  $3\lambda_0$  diameter and  $\epsilon_r = 2.56$ .

TM and TE incident polarizations at a frequency of 300 MHz were considered for each object. Comparisons are made for 2-D RCS in dB-meter (i.e.,  $10 \log_{10}(\sigma_i)$ ). Single-aspect bistatic scattering from  $\theta = 0^\circ$  (forward scatter) to  $\theta = 180^\circ$  (backscatter) is considered for all cases except the last, which compares multiple-aspect monostatic RCS. Since  $\lambda_0 = 1$  m, RCS plots also represent normalized  $\sigma_i/\lambda_0$  for frequency scaled calculations.

Calculations were performed on a 33 MHz, 80486-based personal computer using an extended DOS Fortran-77 compiler. Memory required for these computations was less than 4 MB. The finite element mesh was adjusted to give triangular elements having typical side dimensions of  $\lambda/20$  within the material. For the semi-circular shell shown in Fig. 1, the actual mesh used for the  $2\lambda_0$  diameter example to be considered had about 16 times as many elements as is depicted. For the examples to be considered, computation times averaged about 2 min for the forward operator construction (finite element solution) while the feedback operator integrations required up to an hour. Reduction of the feedback operator integration bottleneck will be discussed in the Conclusion.

Bistatic RCS computations are shown in Fig. 3 for a dielectric circular cylinder with diameter of  $3\lambda_0$  and  $\epsilon_r = 2.56$ . The  $F^3$  calculation (denoted by F3) is compared to that found using a cylindrical harmonic (CH) series algorithm whose coefficients are evaluated by orthogonal Fourier mode matching of the tangential field components at the circular boundary [19].

A two-region bisected cylinder of  $2\lambda_0$  diameter, where left-half  $\epsilon_r = 2$  and right-half  $\epsilon_r = 4$ , is considered in Fig. 4. Comparison RCS was calculated using a specially developed CH program which employs separate left and right region cylindrical harmonic expansions. Full exterior domain expansions are used for the known incident field and the unknown scattered field. The special CH algorithm performs weighted integral (moment) matching of the tangential field components at the circular and bisection boundaries. Since the modes in the various regions are no longer fully orthogonal, as is the case for the homogeneous circular cylinder, a moment matrix system must be filled and inverted to evaluate the expansion coefficients.

Scattering computations for a half-circular dielectric cylinder having  $2\lambda_0$  diameter and  $\epsilon_r = 4$ , is displayed in Fig. 5. Comparison computations were made by the same CH program used for the two-region cylinder in Fig. 4, but with the left-half  $\epsilon_r = 1$ . Strong convergence of the CH and  $F^3$  algorithms, coupled with the good agreement shown in both Figs. 4 and 5, indicate that excellent accuracy is likely being achieved by both approaches.

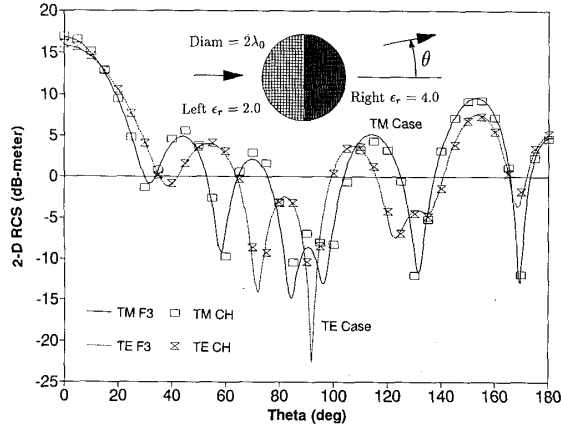


Fig. 4. Comparison of bistatic RCS for a two-region dielectric cylinder having  $2\lambda_0$  diameter, left-half  $\epsilon_r = 2$ , and right-half  $\epsilon_r = 4$ .

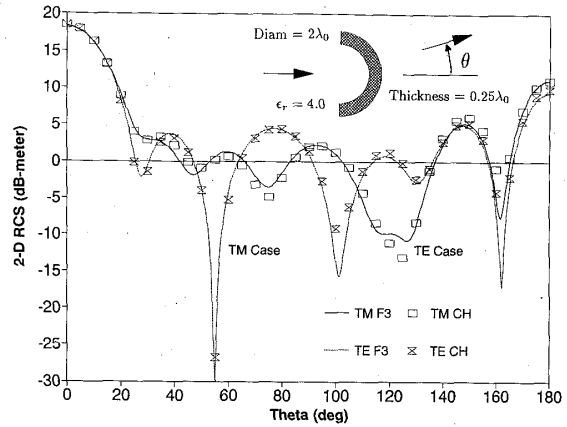


Fig. 6. Comparison of bistatic RCS for a semicircular dielectric shell with thickness  $= 0.25\lambda_0$ , outer diameter  $= 2\lambda_0$  and  $\epsilon_r = 4$ .

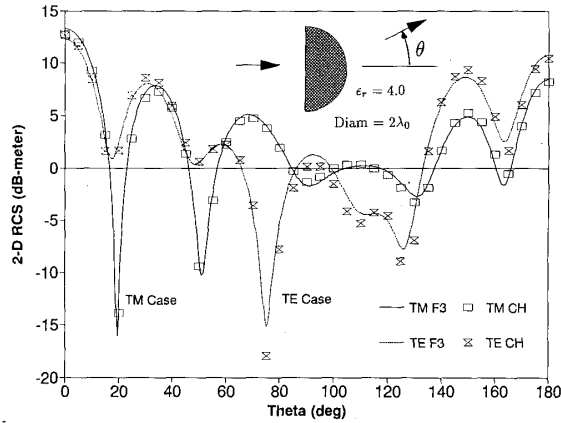


Fig. 5. Comparison of bistatic RCS for a half-circular dielectric cylinder having  $2\lambda_0$  diameter and  $\epsilon_r = 4$ .

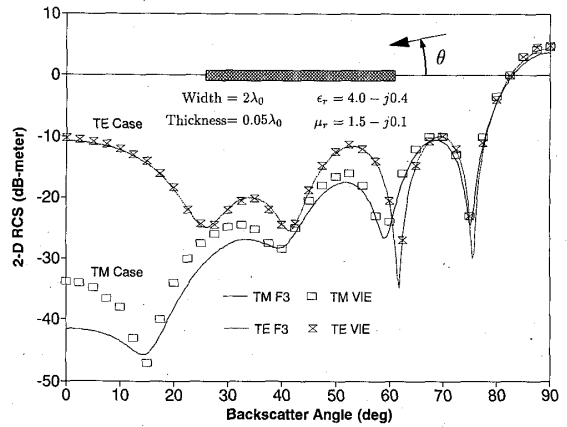


Fig. 7. Comparison of monostatic RCS for a thin lossy planar strip with width  $= 2\lambda_0$ , thickness  $= 0.05\lambda_0$ ,  $\epsilon_r = 4.0 - j0.4$ , and  $\mu_r = 1.5 - j0.1$ .

Next, an example for scattering by a dielectric ( $\epsilon_r = 4$ ) semicircular shell of outer radius  $1.0 \lambda_0$ , and inner radius  $0.75 \lambda_0$ , is shown in Fig. 6. Yet another special case CH program was developed to provide comparison RCS. This algorithm adds two additional vacuum filled regions to the shell to produce a circular cylindrical region of radius  $1.0 \lambda_0$ . These added free-space regions are a left semicircular shell, which complements the right shell, and a circular core of radius  $0.75 \lambda_0$ . CH expansions of the proper form are employed in each of the subregions, including that exterior to the outer radius. Moment matching is performed at the inner and outer circular boundaries, and at the vertical segments between the left and right semicircular shells. As with the bisected cylinder, a full moment matrix system results for the unknown expansion coefficients. Solution convergence was readily achieved for this CH program and superb agreement was observed in comparing to volume integral equation results from Richmond [20].

A final validation is shown in Fig. 7, for the case of a lossy ( $\epsilon_r = 4.0 - j0.4$  and  $\mu_r = 1.5 - j0.1$ ) thin planar strip of width  $2\lambda_0$  and  $0.05\lambda_0$  thickness. Comparisons are made to monostatic 2-D RCS provided by Baucke [21], using a volume integral equation (VIE) approach. Agreement is good for all aspects except near end-on for the TM case, where the RCS is about three orders of magnitude smaller than that for the TE case.

CONCLUSION

Theory and validations of the F3 have been presented for scattering by penetrable 2-D objects. RCS comparisons have been shown for a variety of structures having moderate electrical dimensions.

In applying the  $F^3$ , the forward and feedback matrix operators are computed independently and the scattering solution is then assembled by either iterative or direct procedures. This decoupling of the interior and exterior domains permits limited modifications to the shape and composition of the scattering object, when bounded by fixed mesh contours, while retaining the same feedback matrix. Field feedback system topology also clearly delineates the source of stability problems and ill-conditioning for high-Q scatterers near internal resonance frequencies.

Further enhancements of the  $F^3$  are being pursued. As with integral equations, near-singular behavior of the integrand for terms on, and near, the diagonal of the feedback matrix requires careful and computationally tedious evaluation when direct numerical integration is used. Analytical evaluation of the singular portion of the integration is possible [22], thus reducing the segmentation required for the remaining integration. Going a step further, tests were run [12], which excluded integration contributions outside of a large neighborhood of the field point. These trials indicated that exclusion

beyond a distance of  $1.0 \lambda_0$  yields errors of between 1 and 2% in the integration. Such integration termination could yield significant computational savings when electrically large scatterers are considered.

An exciting area of progress in computational electromagnetics is in the development of radiation boundary conditions (RBC's) which are based upon local differential operator approximations to the behavior of outbound radiation fields. Since the  $F^3$  uses exact analytical field relationships, it provides a starting point to develop new RBC's having innate flexibility and error control.

#### REFERENCES

- [1] K. K. Mei, M. A. Morgan, and S. K. Chang, "Finite methods in electromagnetic scattering," in *Electromagnetic Scattering*, P. L. E. Ushlenghi, Ed. New York: Academic, 1978, ch. 10.
- [2] R. F. Harrington, *Field Computation by Moment Methods*. New York: Macmillan, 1968.
- [3] P. Bettess, "Infinite elements," *Int. J. Num. Meth. Eng.*, vol. 11, pp. 53-64, 1977.
- [4] K. K. Mei, "Unimoment method of solving antenna and scattering problems," *IEEE Trans. Antennas Propagat.*, vol. AP-22, pp. 760-766, Nov. 1974.
- [5] M. A. Morgan and K. K. Mei, "Finite element computation of scattering by inhomogeneous penetrable bodies of revolution," *IEEE Trans. Antennas Propagat.*, vol. AP-27, pp. 202-214, May 1979.
- [6] K. L. Wu, G. Y. Delisle, D. G. Fang and M. Lecours, "Coupled finite element and boundary element methods in electromagnetic scattering," in *Finite Element and Finite Difference Methods in Electromagnetic Scattering*, M. A. Morgan, Ed. New York: Elsevier Science, 1990, ch. 3.
- [7] M. A. Morgan, C. H. Chen, S. C. Hill, and P. W. Barber, "Finite element-boundary integral formulation for electromagnetic scattering," *J. Wave Motion*, vol. 6, pp. 91-103, Jan. 1984.
- [8] R. Mittra and O. Ramahi, "Absorbing boundary conditions for the direct solution of partial differential equations arising in electromagnetic scattering problems," in *Finite Element and Finite Difference Methods in Electromagnetic Scattering*, M. A. Morgan, Ed. New York: Elsevier Science, 1990, ch. 4.
- [9] T. G. Moore, J. G. Blaschak, A. Taflove, and G. A. Kriegsmann, "Theory and application of radiation boundary operators," *IEEE Trans. Antennas Propagat.*, vol. 36, pp. 1797-1812, Dec. 1988.
- [10] R. Janaswamy, "On the applicability of OSRC method to homogeneous scatterers," *IEEE Trans. Antennas Propagat.*, vol. 39, pp. 862-867, June 1991.
- [11] M. A. Morgan and B. E. Welch, "The field feedback formulation for electromagnetic scattering problems," *IEEE Trans. Antennas Propagat.*, vol. AP-34, pp. 1377-1382, Dec. 1986.
- [12] T. B. Welch, "Electromagnetic scattering from two-dimensional objects using the field feedback formulation," Electrical Engineer's Thesis, Elec. Comput. Eng. Dept., Naval Postgraduate School, Monterey, CA, Mar. 1989.
- [13] R. Mittra and C. A. Klein, "Stability and convergence of moment method solutions," in *Numerical and Asymptotic Techniques in Electromagnetics*, R. Mittra, Ed. New York: Springer-Verlag, 1975, ch. 5.
- [14] M. A. Morgan, "Principles of finite methods in electromagnetic scattering," in *Finite Element and Finite Difference Methods in Electromagnetic Scattering*, M. A. Morgan, Ed. New York: Elsevier Science, 1990, ch. 1.
- [15] J. A. Stratton, *Electromagnetic Theory*. New York: McGraw-Hill, 1941, pp. 349-354.
- [16] P. M. Morse and H. Feshbach, *Methods of Theoretical Physics*. New York: McGraw-Hill, 1953, pp. 275-280.
- [17] L. Lapidus and G. F. Pinder, *Numerical Solution of Partial Differential Equations in Science and Engineering*. New York: Wiley Interscience, 1982, ch. 2 and 3.
- [18] J. Van Bladel, *Electromagnetic Fields*, New York: McGraw-Hill, 1964; (Reprinted) New York: Hemisphere, 1985, pp. 372-375.
- [19] D. E. Barrick, "Cylinders," in *Radar Cross Section Handbook*, vol. 1, G. T. Ruck, Ed. New York: Plenum, 1970, ch. 4.
- [20] J. H. Richmond, "TE-wave scattering by a dielectric cylinder of arbitrary cross-section shape," *IEEE Trans. Antennas Propagat.*, vol. AP-14, pp. 460-464, July 1966.
- [21] R. C. Baucke, "Scattering by two-dimensional lossy, inhomogeneous dielectric and magnetic cylinders using linear pyramid basis functions and point matching," *IEEE Trans. Antennas Propagat.*, vol. 39, pp. 255-259, Feb. 1991.
- [22] R. A. Rostant, "Efficient technique for calculating near-fields due to 2-D sources," Master's thesis, Elec. Comput. Eng. Dept., Naval Postgraduate School, Monterey, CA, Dec. 1990.

## High Frequency Inverse Scattering and the Luneberg-Kline Asymptotic Expansion

Michael L. Walker and J. William Helton

**Abstract**—The problem of estimating the relative distances to individual scatterers within a complicated multiscatterer target from radar backscattered signals is addressed. The scattered signal amplitudes produced by these scatterers is estimated. Such information can be useful for detection and identification of targets. An extension is described of the linear prediction algorithm for estimating these quantities applied to a signal model given by the Luneberg-Kline asymptotic expansion for electromagnetic scattering. This model includes the geometrical optics signal model as a special case.

### I. INTRODUCTION

This communication addresses the problem of estimating the relative distances to individual scatterers within a complicated multiscatterer target and their scattered signal amplitudes from radar backscattered signals. The immediate application of this problem is to ultra-high range resolution radar—high resolution radar with potential resolution on the order of feet or inches. This application has significant potential for use in detecting and identifying military and civilian air and ground vehicles. A common method of estimating scatterer location with existing radars is to sample the frequency response of a target over some large bandwidth, then apply a Fourier transform to obtain an approximation to the impulse response of the target (often referred to as "FFT pulse-compression"). Signal peaks extracted from this impulse response are used to estimate individual scatterer distances and scattered signal amplitudes. For a number of practical reasons, sampling is often done at fairly high frequencies, which serves to emphasize the high frequency components of the impulse response. Even the high frequency components of the signal cannot be obtained with arbitrary accuracy, however, due to the necessarily "bandlimited" nature of the data which is collected. In particular, the smoothing of the impulse response caused by convolution due to the finite-length frequency window can "merge" distinct target scatterers (signal peaks). Thus the resolution, or ability to separate distinct target scatterers, obtained via FFT pulse-compression is limited by the practical achievable bandwidth.

Our approach starts with a parametric model of the frequency response. Using the measured frequency response samples, we estimate the model parameters representing the distances to individ-

Manuscript received October 25, 1990; revised December 3, 1991. This work was supported in part by grants from the Air Force Office of Scientific Research and the National Science Foundation.

The authors are with the Department of Mathematics, University of California, San Diego, La Jolla, CA 92093-0012.

IEEE Log Number 9106614.